

Suzaku observations of the hard X-ray spectrum of Vela Jr. (SNR RX J0852.0–4622)

**Sawako TAKEDA,¹ Aya BAMBA,² Yukikatsu TERADA,¹ Makoto S. TASHIRO,¹
Satoru KATSUDA,³ Ryo YAMAZAKI,² Yutaka OHIRA,² and Wataru IWAKIRI⁴**

¹Graduate School of Science and Engineering, Saitama University, Shimo-Okubo 255,
Sakura, Saitama 338-8570

²Graduate School of Science and Engineering, Aoyama-Gakuin University, 5-10-1
Fuchinobe, Chuo, Sagamihara 252-5258

³Department of High Energy Astrophysics, Institute of Space and Astronomical Science
(ISAS), Japan Aerospace Exploration Agency (JAXA), 3-1-1 Yoshinodai, Sagamihara
229-8510

⁴RIKEN (The Institute of Physical and Chemical Research) Nishina Center, 2-1 Hirosawa,
Wako 351-0198

*E-mail: takeda@heal.phy.saitama-u.ac.jp

Received ; Accepted

Abstract

We report the results of Suzaku observations of the young supernova remnant, Vela Jr. (RX J0852.0–4622), which is known to emit synchrotron X-rays, as well as TeV gamma-rays. Utilizing 39 Suzaku mapping observation data from Vela Jr., a significant hard X-ray emission is detected with the hard X-ray detector (HXD) from the north-west TeV-emitting region. The X-ray spectrum is well reproduced by a single power-law model with the photon index of $3.15^{+1.18}_{-1.14}$ in the 12–22 keV band. Compiling this with the soft X-ray spectrum simultaneously observed with the X-ray imaging spectrometer (XIS) onboard Suzaku, we find that the wide-band X-ray spectrum in the 2–22 keV band is reproduced with a single power-law or concave broken power-law model, which are statistically consistent with each other. Whichever the model of a single or broken power-law is appropriate, clearly the spectrum has no rolloff structure. Applying this result to the method introduced in Yamazaki et al. (2014), we find

that one-zone synchrotron model with electron spectrum having a power-law plus exponential cutoff may not be applicable to Vela Jr.

Key words: ISM: supernova remnants — ISM: individual objects (Vela Jr.) — acceleration of particles

1 Introduction

Several supernova remnants (SNRs) are known as sites of acceleration of cosmic-ray particles with the energy of up to TeV. The first observational evidence is discovered by Koyama et al. (1995) in the X-ray band. They found X-rays from shell regions of SN 1006 with ASCA, and revealed that the X-rays are produced via synchrotron radiation by TeV electrons.

We have not yet succeeded observationally in determining the maximum energy and acceleration efficiency of protons and even electrons, which are the key to understand the acceleration site of Galactic cosmic rays. In the context of diffusive shock acceleration, particles with a higher energy require a longer acceleration time, while they have a shorter cooling and escape time (e.g. Drury 2011, Lagage & Cesarsky 1983). These timescales are functions of a diffusion coefficient of accelerated particles around the shock (Bell 1987 and Ohira et al. 2010). Curvature in X-ray synchrotron spectrum depends on the energy spectrum of highest-energy electrons there. Measuring the spectral shape (i.e., slope or photon index, rolloff frequency and spectral curvature) expected to be observed in the X-ray synchrotron emission is crucial to understand the environment and mechanism of cosmic ray acceleration (Yamazaki et al. 2014, Yamazaki et al. 2015).

So far wide-band X-ray spectra have been extensively studied in several SNRs; e.g., RX J1713.7–3946 (Takahashi et al. 2008, Tanaka et al. 2008), SN 1006 (Bamba et al. 2008), Cassiopeia A (Maeda et al. 2009), and G1.9+0.3 (Zoglauer et al. 2015). Rolloff frequencies are reported from a number of SNRs. Bamba et al. (2005a) reported the rolloff energies distributing 0.07 – 11.6 keV, from Cas A, Kepler SNR, Tycho SNR and RCW 86. Utilizing hard X-ray spectra obtained with NuSTAR, the rolloff energies of > 2 keV and 1.27 ± 0.07 keV were observed from Tycho SNR (Lopez et al. 2015) and G 1.9+0.3 (Zoglauer et al. 2015), respectively. TeV gamma-rays have been also observed from a number of SNRs, which are thought to be produced via inverse Compton scattering of TeV electrons or via π^0 decay process of high-energy protons (e.g., Aharonian et al. 2004).

The young SNR Vela Jr. (RX J0852–4622) was discovered by ROSAT in 1998 (Aschenbach 1998). It is one of TeV-emitting SNRs, and has a diameter of 2° . It overlaps with the south-east portion of much larger and known Vela SNR, and is situated near the pulsar and pulsar wind nebulae

(PWN) of Vela SNR. Vela Jr. has a synchrotron X-ray shell (Slane et al. 2001, Bamba et al. 2005b), which is observed also in radio (Combi et al. 1999) and gamma-rays (Aharonian et al. 2005). Fukui (2013) reported a spatial correlation between the radio emission from molecular clouds around Vela Jr. and TeV gamma-rays. Magnetic field strength at the shock surface of Vela Jr. has been estimated by some authors. While Bamba et al. (2005b) estimated the field strength, $B \sim 5 \times 10^2 \mu\text{G}$ from the thickness of X-ray thin shell taken by Chandra, Kishishita et al. (2013) derived $B \sim 5\text{--}20 \mu\text{G}$, by comparing brightness distribution profile at the shell in 2–10 keV with expected radial profile by Petruk et al. (2011). Lee et al. (2013) constructed 1D spherically symmetric model of non-linear diffusive shock acceleration, and obtained $B \sim 4.8 \mu\text{G}$ from observation results, assuming synchrotron X-rays and cosmic microwave background photon upscattered to TeV gamma-rays. The observed spectral slope is so steep that we naturally expect that the synchrotron rolloff energy is below 1 keV, and the spectrum becomes much softer for higher energy bands. However, the synchrotron emission above 10 keV has not been observed for Vela Jr., and thus the spectral shape has not yet been determined. In order to determine the photon index and to examine the expected rolloff structure, wideband X-ray observation covering above 10 keV is important. X-ray astronomy satellite Suzaku (Mitsuda et al. 2007) covers the energy range of 0.2–600 keV with four units of the X-ray Imaging Spectrometers (XISs: Koyama et al. 2007) and the Hard X-ray Detector (HXD: Takahashi et al. 2007). Since both instruments have very low-background capabilities (Tawa et al. 2008; Fukazawa et al. 2009), which enable us to perform high sensitivity surveys of X-rays, the Suzaku is most suitable for diffuse objects. We report the first result of spectral analysis of wideband observation of Vela Jr. with Suzaku. We describe Suzaku observations and data reduction of Vela Jr. in section 2, summarize results of analysis in section 3, and present a discussion in section 4.

2 Observation and Data Reduction

We performed 40 mapping observations of Vela Jr. and its close vicinity in 2005 December, 2007 July, and 2008 July. Table 1 shows the observation details. Hereafter, we refer to each observation position in an abbreviated style by clipping each object name. For example, we call Vela Jr P1 as P1, and RXJ_0852–4622_NW as NW.

One of the two types of instruments of Suzaku is a set of the XISs, each of which is installed on the focal plane of an individual set of the X-ray telescopes (XRTs: Serlemitsos et al. 2006¹). The XIS covers a field of view (FOV) of $17'.8 \times 17'.8$ with the angular resolution of $2'$ in half power diameter in the energy range of 0.2–12 keV. The XIS 0, 2, and 3 are front side illuminated (FI) CCDs,

¹ <http://www.astro.isas.ac.jp/suzaku/doc/suzakumemo/suzakumemo-2006-34.pdf>

whereas XIS 1 is a back-side illuminated (BI) CCD. FI CCDs are more sensitive in the energy band above 5 keV because the depletion layers are thicker than that of a BI CCD. We use only XIS 0, 1, and 3 data because XIS 2 has not been operated since 2007. Spaced-row charge injections (Nakajima et al. 2008, Uchiyama et al. 2009) were carried out in all the observations except NW and NW_offset. We use the software package Heasoft 6.12 with CALDB 2009-08-04 for the analysis and XSPEC v12.7.1 for the spectral analysis². Each observation data is reprocessed by aepipeline 1.0.1. We extract events based on the following criteria: elevation angle from night earth $> 5^\circ$, elevation angle from day earth $> 20^\circ$. We remove calibration source regions at the corner of the FOV.

The HXD is a well-type phoswich counter, whose main detection-part consists of silicon detectors and GSO crystal scintillators. The silicon PIN type semiconductor detector covers hard X-ray band of 10–70 keV, and has FOV of $34' \times 34'$. The GSO crystal scintillators cover the band of 40–600 keV. We do not present the result of GSO because no significant detection is made. Since the well-type active shield provides low-background environment for the PIN detector, it is one of the ideal detectors to observe low surface-brightness objects like SNRs. We extract events which have an elevation angle of $> 5^\circ$ and geomagnetic cut-off rigidity of > 6 GV.

3 Spectral analysis

3.1 XIS

We begin with the analysis of the XIS data. Figure 1 shows the mosaiced XIS image of Vela Jr. in 2–5 keV, which is created with ximage, combining the exposure and vignetting-effect corrected image of each observation. Shell structures of Vela Jr. are clearly visible. We focus on the NW shell which is detected in TeV gamma-rays (Katagiri et al. 2005) and reportedly shows bright synchrotron X-ray filaments (Bamba et al. 2005b). In order to match the data with those of the HXD-PIN, we selected the region inside the FOV of the PIN NW observation which is a square sky region with apexes of (133.37, -45.69), (132.17, -46.45), (131.09, -45.61) and (132.29, -44.86) in equatorial coordinates. Consequently, the entire regions of NW, P1, P2, P3, P4, P11 and P12, and parts of P5, P6, P9, P10, P13, P14, P15, P16 and P17 are included. The spectra are summed with mathpha in units of counts without exposure weighting. The errors are propagated as Poisson errors. Response files are created with marfrmf from redistribution matrix files (rmfs) made by xisrmfgen and ancillary response files (arfs) made by xissimarfgen (Ishisaki et al. 2007), based on the XIS 2–5 keV image file within the FOV of the PIN NW observation. We add all the XIS responses of each observation with the weight of each exposure.

² <https://heasarc.gsfc.nasa.gov/xanadu/xspec/>

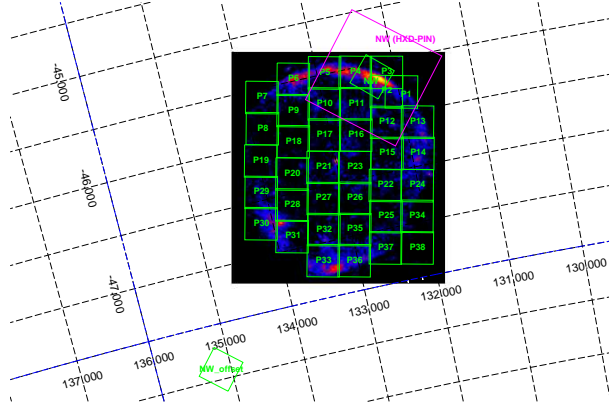


Fig. 1. The mosaiced XIS image of Vela Jr. in 2–5 keV band. The exposure is corrected, but the CXB is not subtracted. The regions of the calibration sources are removed. The green and magenta boxes show the FOVs of the XIS of all the observations and of the PIN during NW observation, respectively. The coordinates are in the J2000 equatorial system.

Since the object extends toward the outside of XIS FOV, we should evaluate background spectra carefully. We here employed the XIS spectra from the observation RXJ_0852–4622_NW_offset (table 1: NW_offset) as the background spectra. However, we must consider the difference in NXB by the difference of the observation days. The NW_offset spectra were obtained in winter of 2005, while the source spectra are the sum of observations in winter of 2005 and summer of 2007. In order to evaluate the possible temporal variation of NXB, we made background spectra (A) by replacing NXB component. The NXB component of each occasion is reproduced by `xisnxbgen` which makes use of the NXB database of the night-earth observations by Tawa et al. (2008) extracting the data from 4 months before to 16 months after an observation. In addition, to examine possible contaminate source in NXB_offset FOV, we compare the background spectra with the NXB plus the CXB estimated by Kushino et al. 2002 (B). Above backgrounds are summarized in figure 2 and we confirmed the background spectra are consistently reproduced within the errors. Then, we safely adopt the NW_offset background ignoring the energy range of 5.9 ± 0.2 keV also to eliminate scattered ^{55}Fe line from the decaying calibration source during the observations.

We evaluate background-subtracted XIS spectra by fitting with a power-law function with the Galactic absorption: `phabs*powerlaw`. The absorption column density is fixed to be $6.7 \times 10^{21} \text{ cm}^{-2}$, which is the best-fit value derived by Hiraga et al. (2009), with the metal abundance adopted from Anders & Grevesse (1989). We ignore the energy range of below 2 keV to avoid thermal contamination from Vela SNR (Hiraga et al. 2009). Figure 3 shows the XIS spectra, and Table 2 shows the best-fit parameters.

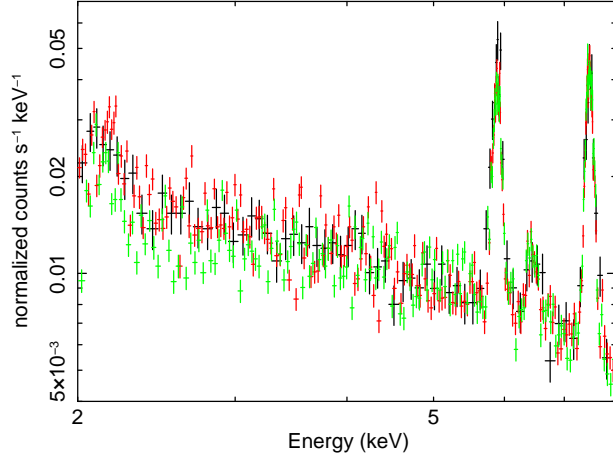


Fig. 2. Background spectrum of the XIS 0 in 2.0–8.0 keV band. The black, red, and green lines denote the NW_offset, the NXB-replaced background (A), and the simulated NXB plus modeled CXB (Kushino et al. 2002) background (B), respectively.

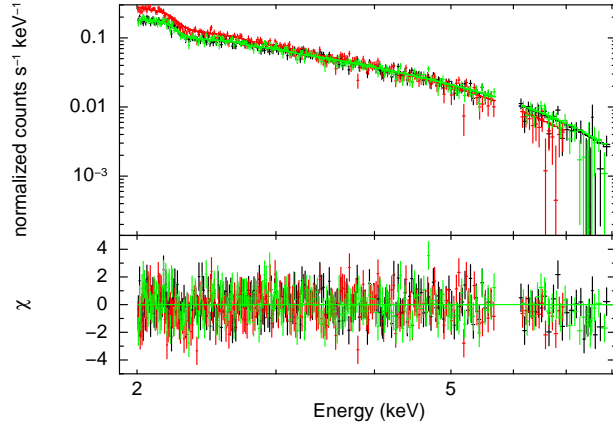


Fig. 3. The upper panel shows the XIS spectra fitted with a single power-law model in the 2.0–8.0 keV band. The lower panel shows the χ^2 -residuals between the data and best-fit model. The black, red, and green lines denote the XIS 0, 1, and 3 data, respectively.

3.2 HXD-PIN

To identify pointings which show significant hard X-ray signals with HXD-PIN, we compare the background-subtracted count-rates of each observation with the systematic error of the corresponding simulated background spectrum. We employ a modeled CXB by Boldt & Leiter (1987) and simulated NXB spectrum with `hxdpinxbpi`, the latter of which is calculated on the basis of observed NXB spectrum during earth occultation. The expected uncertainty of the NXB model is reported as 3% in 10–60 keV by Fukazawa et al. (2009). The PIN detection significance is determined with the NXB reproducibility. Since hard X-ray sources RCW 38 and IGR J09026–4812 contaminate the NW_offset observation, those offset observations are not to be used to estimate the NXB and CXB backgrounds for this HXD-PIN analysis. We ignore the energy band below 12 keV to avoid thermal noise. Consequently, we obtain 6 observations that exceed 1σ significance level of NXB uncertainty in the

10–60 keV band: P1, P2, P3, P5, P13, and NW, all of which are located in the north-west of Vela Jr.

To confirm the detections, we re-evaluate uncertainty of the NXB model for each observation by comparing the count rate of CXB-subtracted signal with that of each simulated NXB in the 10–60 keV band. For the NXB, we derive the count rate during earth occultations during each observation. All but the NW contained some periods of earth occultations. For the NW observation, we used the earth occultation data obtained in the observations conducted immediately before and 26 hours after the NW observation: E0102–72 (ObsID 100044010) and NGC 4388 (ObsID 800017010). Comparing those with the count rate of the model, we estimate the systematic uncertainties of the NXB model to be $\sim 7\%$, 6% , 0.2% , 0.5% , 9% , and 1% for positions P1, P2, P3, P5, P13, and NW, respectively, in 10–60 keV. P1, P2, and P13 have larger uncertainty than the nominal value reported in Fukazawa et al. (2009) because the exposures of earth occultation were short. A significant emission to 21.9 keV from the position NW is detected at 3σ confidence level, whereas those from the other observations are detected at only $0.5\text{--}1.5\sigma$ level.

In order to examine the PIN spectrum of diffuse objects, we need to calculate the effective areas for which the angular response is convolved (‘arf’ in the XSPEC), based on the source brightness distribution within the FOV. We assume that the spatial distribution in the hard X-ray band with PIN is the same as the CXB-subtracted XIS 2–5 keV images (section 3.1). The proper response of the PIN detectors has a pyramidal shape. However, for simplicity, we divide the spatial distribution within the PIN FOV by 9×9 grids and make 81 arfs in total with `hxdarfgen`, assuming that a point source centered in each section is responsible for the entire flux from the section in making an arf in each section. Then we sum up these arfs with `addarf` with weights calculated from the XIS image. Practically, this procedure is to approximate the original pyramidal angular response by 9×9 prisms. We calculate the ratio of the geometric integrations of the 81 prisms to the pyramid to be 0.8. Thus, the flux based on this arf should come out at the value $1/0.8 = 1.25$ times larger than the real one.

We validate this ratio of the normalizations with another pair of data sets: (A) the effective area derived with this method for the 9×9 section with a uniform weight, (B) that calculated from the numerically-simulated flat-sky response file, which is delivered by the HXD team. We confirm that the ratio of the former (A) to the latter (B) is ~ 0.8 and so is consistent with the value calculated above.

Now that the method is validated, we make the arf for our HXD-PIN spectrum with this method, assuming the HXD-PIN spatial distribution of Vela Jr. to be the same as the CXB-subtracted brightness distribution observed with the XIS. We find that 39 out of the 81 sections inside Vela Jr. show no significant XIS signal and hence give them the weight of zero in calculating the arf for the HXD-PIN spectrum. Figure 4 displays the employed sections, and Table 3 lists the weights. All the

flux and flux values presented hereafter are corrected for the above-mentioned factor.

Using the arf for Vela Jr. NW with the officially delivered responses for the flat sky and a point source, we examine the observed hard X-ray spectrum in detail. First, we evaluate possible contamination of the galactic ridge X-ray emission (GRXE: Krivonos et al. 2007), given the fact that Vela Jr. is on the Galactic plane. We use the NXB-subtracted XIS spectrum of the offset observation as the background template for the HXD data of Vela Jr. We fit it with, in addition to the fixed CXB model (Kushino et al. 2002), the GRXE model, for which we employ a photo-absorbed two temperature thermal plasma emission model. Assumed absorption column density $N_{\text{H}} = 4.0 \times 10^{22} \text{cm}^{-2}$ and the two temperature thermal plasma model (apec in XSPEC) with $kT = 1.66 \text{ keV}$ and 15.1 keV (Table 4 of Yuasa et al. 2012). Considering the effective solid angle of PIN and XIS, we then estimate the GRXE component flux for the PIN spectrum (12 – 22 keV) and XIS spectrum (2 – 10 keV) to be 2.00×10^{-13} and $7.01 \times 10^{-13} \text{ erg cm}^{-2} \text{s}^{-1}$, respectively. This estimated GRXE model is included in all the following model-fittings of the HXD-PIN spectrum. Note that the flux of GRXE in the XIS range is 2% of that from NW. Therefore, the effect of the GRXE to the XIS spectrum is negligible.

Second, we check the possible contamination from nearby hard X-ray sources. According to the INTEGRAL catalog³, there was no contaminating point-source in the 18.3–59.9 keV range in the FOV of the HXD-PIN. The brightest diffuse source in the PIN FOV is Vela PWN below 10 keV (Katsuda et al. 2011). Mori et al. (2014) studied the spectrum of Vela PWN with the XIS observation of VELA PWN E7 (ObsID 506050010), and reported that the surface brightness is ~ 0.3 times CXB level and that the photon index is ~ 3.3 . This flux corresponds to 5% of that of the NW in the 2–10 keV band, and hence our XIS spectrum is not significantly affected with the Vela PWN component within statistics. Extrapolating this spectrum to the energy band of the HXD-PIN, we find that the flux of Vela PWN is $\leq 2\%$ of that of the NW in the 12–22 keV energy range, and therefore the contribution from the Vela PWN component is negligible for the PIN data. Therefore, we conclude that the detected signals are fully originated from Vela Jr. NW.

Finally we fit the background-subtracted HXD-PIN spectrum up to 22 keV with a single power-law model. Figure 5 shows the spectrum with the best-fit model. The systematic error of the NXB model of 1%, which is derived based on the earth occultation data, is included in errors of the source spectrum. The spectrum is well reproduced by a single power-law model with $\chi^2/\text{d.o.f.} \sim 0.22$. The best-fit photon index is $3.15^{+1.18}_{-1.14}$ and the flux is $(8.26 \pm 1.44) \times 10^{-12} \text{ erg cm}^{-2} \text{s}^{-1}$ in 12–22 keV, as listed in table 2. Here the errors due to the model-fitting error of the GRXE are 0.006% for the photon index and 0.02% for normalization.

³ <http://www.isdc.unige.ch/integral/science/catalogue>

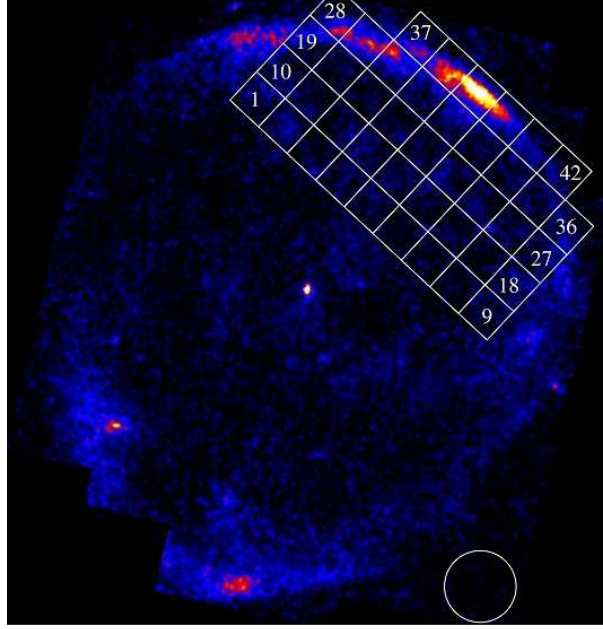


Fig. 4. Forty-two white boxes used to estimate the arf, in which the significant X-ray emission was detected with the XIS (see text). A white circle is the region for estimating the background. The image is the same as Figure 1.

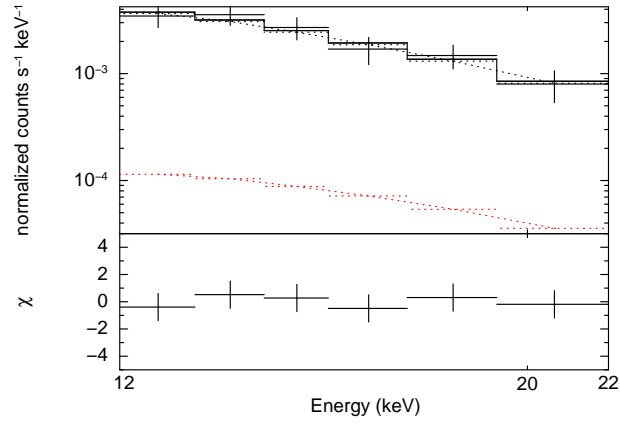


Fig. 5. The black points in the upper panel show the HXD-PIN spectrum fitted with single power-law model in 12.0–22.0 keV band. The error bars include also the systematic error of the NXB model. The red dotted line shows the contribution from the modeled GRXE. The lower panel shows the χ residuals between the data and best-fit model.

3.3 Wide-band spectrum

In sections 3.1 and 3.2, we have derived the spectral parameters independently with the XIS and PIN. We then fit the XIS and PIN spectra simultaneously to give further constraints, making use of the best available statistics.

First, we apply a single power-law model, referred to as model (i) in Table 4, linking the photon index for the XIS and PIN spectra. Ishida et al. (2007)⁴ reported that the normalization factors differed between the XIS and PIN spectra for the point-like source Crab, which has a power-law spectrum, and that their ratio of the PIN to the XIS (henceforth referred to as the cross-normalization) was 1.13. Thus, we link the power-law normalizations of the XIS and PIN spectra with the ratio of 1/1.13 in the model-fitting. Figure 6 shows the spectra and the best-fit model, and Table 4 lists the best-fit parameters.

The X-ray spectra of several SNRs have rolloff structures (e.g. Takahashi et al. 2008, Tanaka et al. 2008, Bamba et al. 2008, Zoglauer et al. 2015). Although the above result on a single power-law model does not require any spectral bending in the 2–22 keV band, we further try to examine a possible spectral curvature with various models listed in Table 4, setting the cross-normalization to 1.13 (see the previous sub-section). Table 4 shows the best-fit parameters of each model. Four panels in figure 6 show the spectrum overlaid with the best-fit model spectra for 4 different models. The parameters with the cutoff power-law (`cutoffpl` in XSPEC) which is a power-law model with high energy exponential rolloff (ii) are consistent with the results with the single power-law model (i), because the lower limit of rolloff energy of 131 keV is out of the range. Fitting with the broken power-law model (iii; `bknpower` in XSPEC) implies the breaking energy of 7.90 ± 0.18 keV with a change of spectral index of -0.3 , although it is still consistent with the results of individual fittings with the XIS and PIN, and with the wide-band fittings with the models (i) and (ii), within errors.

⁴ <http://www.astro.isas.ac.jp/suzaku/doc/suzakumemo/suzakumemo-2007-11.pdf>

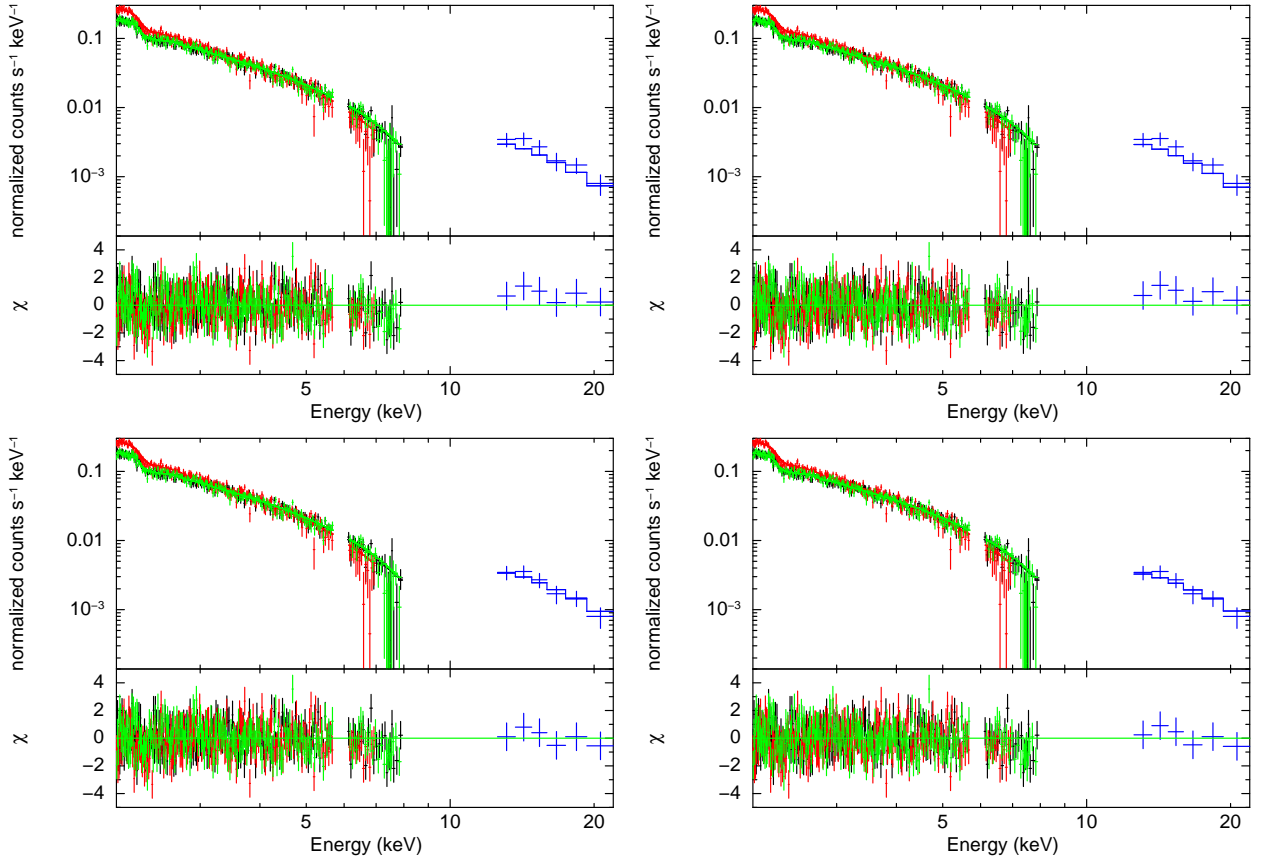


Fig. 6. Upper left: The upper panel shows the wide band spectrum fitted with (i) single power-law model in 2.0–22.0 keV band. The systematic error of NXB model is included. The cross normalization is fixed at 1.13, which is the value for a point source. The lower panel shows the residuals between the data and model. Upper right: Same as the upper left except for using (ii) cutoff power-law model. Lower left: Same as the upper left except for using (iii) broken power-law. Lower right: Same as the upper left except for using (iv) 10 keV broken power-law.

4 Discussion and Summary

In section 3, we have shown the results of spectral analysis of Vela Jr. with Suzaku. X-rays with the energy up to 22 keV are detected from the north-west region of Vela Jr. The spectra in the soft and hard X-ray band are reproduced with a power-law model with the photon indices of 2.93 ± 0.02 and $3.15^{+1.18}_{-1.14}$, respectively. When the spectra in both the bands are fitted simultaneously, a single power-law model with the photon index of 2.92 ± 0.01 , or a slightly concave-shaped broken power-law model, is accepted.

The obtained wide band steep power-law like spectrum with photon index ~ 3 implies the energy index $p \sim 5$ of synchrotron electron with the energy distribution of $dN/dE \propto E^{-p}$. This steep spectrum strongly suggests that the rolloff energy is well below the XIS band. Combi et al. (1999) reported the radio spectral index of $\alpha = 0.3 \pm 0.3$ at NW region, and Duncan et al. (2000) reported the flux density at 1 GHz of ~ 50 Jy from entire region of the SNR. In order to verify consistency between the X-ray and radio results, the X-ray spectra with XIS and PIN are tested with srcut model in

XSPEC (Reynolds 1998). The `srcut` model describes the synchrotron spectrum from electrons with an exponentially-rolloff power-law distribution in energy. The synchrotron spectrum has a power-law form from radio band to X-ray band with a rolloff energy. The `srcut` model has three parameters; X-ray rolloff energy, spectral index at 1 GHz, and flux at 1 GHz. We fit the X-ray spectra using spectral index α in radio band reported by Combi et al. (1999) and typical value of young SNRs, i.e., $\alpha = 0.3$ and $\alpha = 0.6$, respectively. Then, when $\alpha = 0.3$, the best fit parameters of 1 GHz flux density and rolloff energy of 0.15 ± 0.01 Jy and 0.15 ± 0.01 keV with $\chi^2/\text{d.o.f.}$ of 1.18. When $\alpha = 0.6$, these are $31.6^{+1.8}_{-1.9}$ Jy and 0.27 ± 0.01 keV with $\chi^2/\text{d.o.f.}$ of 1.17. The area of NW region in this paper is $\sim 27\%$ of entire Vela Jr., hence the 1 GHz flux is expected to become smaller than values reported by Duncan et al. (2000) which is derived from emission of entire Vela Jr. Actually the derived radio flux is smaller than the value of entire Vela Jr. reported by Duncan et al. (2000). In addition, rolloff energy is below the XIS band, which is consistent with our X-ray analysis. Therefore results of our X-ray analysis and in radio band are consistent each other. Since the radio flux at NW region alone has not been reported, additional radio observation is needed to verify this result on wideband spectrum of the NW region.

Thus the steep X-ray spectrum naturally requires concave rolloff structure as far as we assume simple acceleration/synchrotron cooling mechanism. For example, Yamazaki et al. (2014) proposed a simple diagnostic to find possible acceleration mechanisms from the observed spectral shape near the maximum energy, assuming (a) one-zone, (b) electron energy spectrum of an exponential cutoff power-law ($N(E) \propto E^{-p} \exp[-(E/E_{\text{max,e}})^a]$) expressed as equation 1 in Yamazaki et al. (2014), and (c) synchrotron radiation. Figure 5 in Yamazaki et al. (2014) shows the relation between the electron spectral parameters p and a on the relation of soft and hard X-ray spectral indices.

In order to discuss theoretical models, we tried a fitting with a broken power-law model (iv) with the fixed breaking energy to 10 keV. Table 4 shows the best-fit parameters of this model, and lower right panel of Figure 6 is the spectrum overlaid with the best-fit model spectra. Both the derived photon indices are consistent with that obtained with the model (iii), though that in the hard band is marginally smaller by 0.1 than the latter. The best-fit flux is close to that obtained in the models (i) and (ii). Figure 7 overlays our results of the photon indices of below and above 10 keV in the model (iv) in red on Figure 5 in Yamazaki et al. (2014). We find that our data do not fit any of the theoretical-model lines by Yamazaki et al. (2014). Thus we find Vela Jr. is the second outlier of the theoretical lines following Cassiopeia A, despite the spectrum in higher energy than rolloff. They are unlike the other SNR RX J1713.7–3946 whose spectral shape is well described with power-law + exponential cutoff model, exhibits the soft and hard photon indices on one of the theoretical lines.

A possible cause for the mismatch is that at least one of the assumptions (a), (b) and (c) is

incorrect for this object. A normal one-zone synchrotron X-ray spectrum usually has a photon index of ~ 2 in a softer energy band and rolls off toward the harder energy band due to cooling or escape. However the wide-band X-ray spectrum of Vela Jr. is well reproduced with a single power-law or even a concave-shape broken power-law. It may suggest that combination of more than one emission component and/or complex emission mechanisms creates the observed X-ray spectra (Longair 1994, Drury et al. 1999, Zirakashvili & Aharonian 2007, Malkov & Drury 2001, Toptygin & Fleishman 1987, Medvedev 2000, Reville & Kirk 2010, Teraki & Takahara 2011, Yamazaki et al. 2006, Laming 2001, Vink & Laming 2003, Vink 2008, Ohira et al. 2012).

In addition, in order to validate the cross-normalization between the XIS and the PIN, we fit the spectra, allowing both the XIS and PIN normalizations to vary independently, and find that the best-fit photon index and the XIS flux are consistent with the above-discussed case within the error range, whereas the derived cross-normalization factor is 1.4 ± 0.3 , which is marginally larger than that reported for the point source. This result may imply that brightness distribution in hard X-rays is more compact than that of the XIS image and that we have actually underestimated the PIN effective area, as we have assumed a larger diffuse-emission region than the real one. Considering the case of more compact hard X-ray brightness distribution than that of soft X-rays, we also showed a conservative fitting result with freed cross-normalization factor in figure 7 with blue mark and error bars. The best-fit photon indices are 2.93 ± 0.04 and $3.16^{+2.44}_{-2.20}$ in the soft and hard energy range, respectively. Although this estimation accepts most of the model lines presented in Yamazaki et al. (2014), it requires more than one emission region or complex emission mechanisms.

Lastly, we show flux comparison with TeV emission. In section 3.1, we derived the flux of $(4.43 \pm 0.03) \times 10^{-11} \text{ erg cm}^{-2} \text{ s}^{-1}$ in 2–10 keV band while Aharonian et al. (2007) showed the TeV flux of entire Vela Jr. of $(15.2 \pm 0.7 \pm 3.20) \pm 10^{-12} \text{ cm}^{-2} \text{ s}^{-1}$ with H.E.S.S. Both band spectra exhibit similar slope and the X-ray to TeV gamma-ray flux ratio is ~ 2.91 . If we assume the cosmic microwave background inverse Compton scattering as TeV emission mechanism, we estimate the magnetic field $B \sim 5.5 \mu\text{G}$, which is consistent value derived by Kishishita et al. (2013) and Lee et al. (2013). If the TeV emission is hadronic, the field strength is not constrained and it may be much higher (Bamba et al. 2005b).

Acknowledgments

The authors would like to thank all the members of the Suzaku team for their continuous contributions in the maintenance of onboard instruments, spacecraft operation, calibrations, software development, and user support both in Japan and the United States. We would like to thank associate professor Koji Mori for analysis of the XIS image. We would like to thank Prof. Yasushi Fukazawa and Dr. Takaaki Tanaka for useful comments about analysis of HXD-PIN. This work was supported in part by Grants-in-Aid for Scientific Research from the Ministry of Education, Culture, Sports,

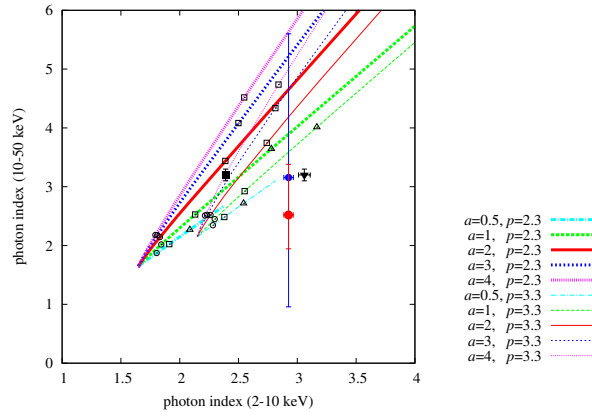


Fig. 7. The relation between the two X-ray photon indices for soft and hard bands for a breaking power-law model. The straight lines show the theoretical lines derived by Yamazaki et al. (2014). The open squares, triangles and circles are for $BE_{\text{max},e}^2 = 10^4$, 10^5 , and $10^6 \mu\text{G}(\text{TeV})^2$, respectively (See Yamazaki et al. 2014). The black squares and triangles show the result of RX J1713.7–3946 and of Cassiopeia A, respectively. The red and blue circles show this result with model (iv) with cross-normalization fixed to 1.13 or freed, respectively. These error bars show 99% confidence level.

Science and Technology (MEXT) (No. 23340055, Y. T, No. 15K05088, R. Y, No. 15K05107, A. B., No. 15H03642-01, M. S. T., and No. 25800119, S. K.).

References

- Aharonian, F., et al. 2004, *Nature*, 432, 75
- Aharonian, F., et al. 2005, *A&A*, 437, 7
- Aharonian, F., et al. 2007, *ApJ*, 661, 236
- Anders, E. & Grevesse, N. 1989, *Geochim. Cosmochim. Acta*, 53, 197
- Aschenbach, B. 1998, *Nature*, 396, 141
- Bamba, A., Yamazaki, R., Yoshida, T., Terasawa, T., & Koyama, K. 2005a, *ApJ*, 621, 793
- Bamba, A., Yamazaki, R. & Hiraga, J. S. 2005b, *ApJ*, 632, 294
- Bamba, A., et al. 2008, *PASJ*, 60, 153
- Bell, A. R. 1987, *MNRAS*, 225, 615
- Boldt, E. & Leiter, D. 1987, *ApJL*, 322, 1
- Combi, J. A., Romero, G. E. & Benaglia, P. 1999, *ApJ*, 519, 177
- Drury, L. O., Duffy, P., Eichler, D. & Mastichiadis, A. 1999, *A&A*, 347, 370
- Drury, L. O. 2011, *MNRAS*, 415, 1807
- Duncan, A. R. & Green, D. A. 2000, *A&A*, 364, 732
- Fukazawa, Y., et al. 2009, *PASJ*, 61, 17
- Fukui, Y. 2013, *Ap&SS*, 34, 249

Hiraga, J. S., et al. 2009, PASJ, 61, 275

Ishisaki, Y., et al. 2007, PASJ, 59, 113

Katagiri, H., et al. 2005, ApJ, 619, 163

Katsuda, S., et al. 2011, PASJ, 63, 827

Kishishita, T., Hiraga, J. & Uchiyama, Y. 2013, A&A, 551, 132

Kokubun, M., et al. 2007, PASJ, 59, 53

Koyama, K., Petre, R., Gotthelf, E. V., Hwang, U., Matsuura, M., Ozaki, M. & Holt, S. S. 1995, Nature, 378, 255

Koyama, K., et al. 2007, PASJ, 59, 23

Krivoson, R., Revnivtsev, M., Churazov, E., Sazonov, S., Grebenev, S., & Sunyaev, R. 2007, A&A, 463, 957

Kushino, A., Ishisaki, Y., Morita, U., Yamasaki, N. Y., Ishida, M., Ohashi, T., & Ueda, Y. 2002, PASJ, 54, 327

Lagage, P. O. & Cesarsky, C. J. 1983, A&A, 125, 249

Laming, J. M. 2001, ApJ, 546, 1149

Lee, S.-H., Slane, P. O., Ellison, D. C., Nagataki, S. & Patnaude, D. J. 2013, ApJ, 767, 20

Longair, M. S. 1994, High energy astrophysics. Volume 2. Stars, the Galaxy and the interstellar medium.

Lopez, L. A. et al. 2015, ApJ, 814, 132

Maeda, Y., et al. 2009, PASJ, 61, 1217

Malkov, M. A. & Drury, L. O. 2001, Reports on Progress in Physics, 64, 429

Medvedev, M. V. 2000, ApJ, 540, 704

Mitsuda, K., et al. 2007, PASJ, 59, 1

Mori, K., Katsuda, S., Uchida, H. & Tsunemi, H. 2014, efxu.conf, 52

Nakajima, H., et al. 2008, PASJ, 60, 1

Ohira, Y., Murase, K. & Yamazaki, R. 2010, A&A, 513, 17

Ohira, Y., Kohri, K. & Kawanaka, N. 2012, MNRAS, 421, 102

Petruk, O., Orlando, S., Beshley, V. & Bocchino, F. 2011, MNRAS, 413, 1657

Reville, B. and Kirk, J. G. 2010, ApJ, 724, 1283

Reynolds, S. P. 1998, ApJ, 493, 375

Slane, P., Hughes, J. P., Edgar, R. J., Plucinsky, P. P., Miyata, E., Tsunemi, H., & Aschenbach, B. 2001, ApJ, 548, 814

Takahashi, T., et al. 2007, PASJ, 59, 35

Takahashi, T., et al. 2008, PASJ, 60, 131

Tanaka, T., et al. 2008, ApJ, 685, 988

Tawa, N., et al. 2008, PASJ, 60, 11

Teraki, Y. and Takahara, F. 2011, ApJL, 735, 44

Toptygin, I. N. & Fleishman, G. D. 1987, *Ap&SS*, 132, 213
 Uchiyama, H., et al. 2009, *PASJ*, 61, 9
 Vink, J. & Laming, J. M. 2003, *ApJ*, 584, 758
 Vink, J. 2008, *A&A*, 486, 837
 Yamazaki, R., Kohri, K., Bamba, A., Yoshida, T., Tsuribe, T. & Takahara, F. 2006, *MNRAS*, 371, 1975
 Yamazaki, R., Ohira, Y., Sawada, M. & Bamba, A. 2014, *RAA*, 14, 165
 Yamazaki, R., Yoshida, T., Tsuchihashi, Y., Nakajima, R., Ohira, Y., & Yanagita, S. 2015, *JHEAp*, 5, 1
 Yuasa, T., Makishima, K., & Nakazawa, K. 2012, *ApJ*, 753, 129
 Zirakashvili, V. N. & Aharonian, F. 2007, *A&A*, 465, 695
 Zoglauer, A., et al. 2015, *ApJ*, 798, 98

Table 1. The basic parameters of the Suzaku observations. The exposures are the ones after processing and of the XIS, unless otherwise noted.

Name	ObsID	Date (YYYY-MM-DD)	RA (deg)	Dec (deg)	Exposure (ks)
VELA JR P1	502023010	2007-07-04	131.98	−45.806	10.7
VELA JR P2	502024010	2007-07-04	132.17	−45.775	8.26
VELA JR P3	502025010	2007-07-04	132.12	−45.604	6.70
VELA JR P4	502026010	2007-07-05	132.52	−45.545	10.3
VELA JR P5	502027010	2007-07-05	132.91	−45.488	10.7
VELA JR P6	502028010	2007-07-05	133.33	−45.485	7.15
VELA JR P7	502029010	2007-07-05	133.78	−45.583	11.8
VELA JR P8	502030010	2007-07-06	133.86	−45.861	13.2
VELA JR P9	502031010	2007-07-06	133.42	−45.763	8.64
VELA JR P10	502032010	2007-07-06	133.00	−45.766	10.2
VELA JR P11	502033010	2007-07-07	132.60	−45.826	11.3
VELA JR P12	502034010	2007-07-08	132.25	−46.051	9.75
VELA JR P13	502035010	2007-07-09	131.85	−46.106	9.41
VELA JR P14	502036010	2007-07-09	131.93	−46.386	10.7
VELA JR P15	502037010	2007-07-10	132.33	−46.329	8.88
VELA JR P16	502038010	2007-07-10	132.68	−46.105	15.1
VELA JR P17	502039010	2007-07-10	133.09	−46.046	7.83
VELA JR P18	502040010	2007-07-10	133.51	−46.042	12.8
VELA JR P19	503031010	2008-07-03	133.98	−46.148	17.7
VELA JR P20	503032010	2008-07-04	133.62	−46.327	13.4
VELA JR P21	503033010	2008-07-04	133.20	−46.330	11.8
VELA JR P22	503034010	2008-07-05	132.44	−46.613	14.7
VELA JR P23	503035010	2008-07-05	132.79	−46.395	10.7
VELA JR P24	503036010	2008-07-05	132.03	−46.673	12.4
VELA JR P25	503037010	2008-07-06	132.52	−46.892	11.4
VELA JR P26	503038010	2008-07-06	132.88	−46.669	10.7
VELA JR P27	503039010	2008-07-06	133.28	−46.606	11.0
VELA JR P28	503040010	2008-07-07	133.71	−46.604	10.9
VELA JR P29	503041010	2008-07-07	134.07	−46.430	8.04
VELA JR P30	503042010	2008-07-07	134.17	−46.704	10.1
VELA JR P31	503043010	2008-07-08	133.80	−46.885	10.6

Table 1. (Continued)

Name	ObsID	Date (YYYY-MM-DD)	RA (deg)	Dec (deg)	Exposure (ks)
VELA JR P32	503044010	2008-07-08	133.37	−46.887	7.64
VELA JR P33	503045010	2008-07-08	133.47	−47.162	11.0
VELA JR P34	503046010	2008-07-09	132.11	−46.950	10.6
VELA JR P35	503047010	2008-07-09	132.97	−46.947	8.65
VELA JR P36	503048010	2008-07-09	133.06	−47.224	9.36
VELA JR P37	503049010	2008-07-09	132.61	−47.170	12.3
VELA JR P38	503050010	2008-07-10	132.20	−47.231	10.4
RXJ_0852−4622_NW	500010010	2005-12-19	132.29	−45.616	161 (XIS) / 215 (PIN)
RXJ_0852−4622_NW_offset	500010020	2005-12-23	135.13	−47.910	54.5

Table 2. The best-fit parameters for a power-law model for the XIS spectra and the PIN spectrum.

Parameter	XIS*	HXD-PIN†
Photon index	2.93 ± 0.02	$3.15^{+1.18}_{-1.14}$
flux [$\text{erg cm}^{-2} \text{s}^{-1}$]	$4.43 \pm 0.03 \times 10^{-11} \ddagger$	$8.26 \pm 1.44 \times 10^{-12} \S$
$\chi^2/\text{d.o.f.}$	732.16/658	0.87/4

Notes. Errors are for a single parameter of interest in 90% confidence.

* The absorbing column density is set to be $6.7 \times 10^{21} \text{cm}^{-2}$, referring to Hiraga et al. (2009).

† The model contains the fixed GRXE component and the normalization is corrected (see text).

‡ The flux at the range of 2–10 keV.

§ The flux at the range of 12–22 keV.

Table 3. The weights for making arfs of the PIN. The pointing IDs are shown in figure 4.

Pointing ID	weight	Pointing ID	weight
1	0.018	22	0.012
2	0.020	23	0.013
3	0.012	24	0.017
4	0.014	25	0.016
5	0.013	26	0.016
6	0.009	27	0.021
7	0.009	28	0.033
8	0.009	29	0.068
9	0.015	30	0.053
10	0.019	31	0.028
11	0.013	32	0.032
12	0.014	33	0.016
13	0.017	34	0.016
14	0.015	35	0.018
15	0.013	36	0.021
16	0.013	37	0.034
17	0.009	38	0.076
18	0.022	39	0.119
19	0.034	40	0.051
20	0.013	41	0.022
21	0.010	42	0.008

Table 4. The best-fit parameters for the XIS and PIN spectra.

Parameters	(i) single power-law	(ii) cutoff power-law	(iii) broken power-law	(iv) 10 keV broken power-law
Photon index (all or soft)	2.92 ± 0.01	2.90 ± 0.01	2.93 ± 0.01	2.93 ± 0.01
Photon index (hard)	–	–	2.66 ± 0.03	$2.56^{+0.42}_{-0.34}$
rolloff energy [keV]	–	> 131	–	–
breaking energy [keV]	–	–	7.90 ± 0.18	10.0 (fixed)
flux _{10keV} [$\times 10^{-5}$ Jy]	5.05 ± 0.03	4.92 ± 0.03	5.30 ± 0.03	4.99 ± 0.03
χ^2 / d.o.f.	736.51/664	735.69/663	733.59/662	733.85/663

Notes. The absorbing column density is set to be $6.7 \times 10^{21} \text{ cm}^{-2}$, referring to Hiraga et al. (2009). Cross-normalization factor of HXD-PIN is fixed at 1.13, which is the value for a point source. Errors are for a single parameter of interest in 90 % confidence.